



**Hot Carriers in Action: Multimodal Photocatalysis on
Au@SnO₂ Core-Shell Nanoparticles**

Journal:	<i>Nanoscale</i>
Manuscript ID	NR-ART-03-2019-002130.R1
Article Type:	Paper
Date Submitted by the Author:	20-Mar-2019
Complete List of Authors:	Fu, Xiaoqi; Jiangsu University, Chemistry and Chemical Engineering Li, Guangfang; University of South Carolina, Department of Chemistry and Biochemistry Villarreal, Esteban; University of South Carolina, Department of Chemistry and Biochemistry Wang, Hui; University of South Carolina, Department of Chemistry and Biochemistry

ARTICLE

Hot Carriers in Action: Multimodal Photocatalysis on Au@SnO₂ Core-Shell Nanoparticles

Received 00th January 20xx,
Accepted 00th January 20xx

Xiaoqi Fu,^{*,a,b} Guangfang Grace Li,^a Esteban Villarreal^a and Hui Wang^{*,a}

DOI: 10.1039/x0xx00000x

Metal-semiconductor hybrid heteronanostructures exhibit intriguing multimodal photocatalytic behaviors dictated by multiple types of photoexcited charge carriers with distinct energy distribution profiles, excited-state lifetimes, and interfacial transfer dynamics. Here we take full advantage of the optical tunability offered by Au@SnO₂ core-shell nanoparticles to systematically tune the frequencies of plasmonic electron oscillations in the visible and near-infrared over a broad spectral range well-below the energy thresholds for the interband transitions of Au and the excitonic excitations of SnO₂. Employing Au@SnO₂ core-shell nanoparticles as an optically tunable photocatalyst, we have been able to create energetic hot carriers exploitable for photocatalysis by selectively exciting the plasmonic intraband transitions and the d→sp interband transitions in the Au cores at energies below the band gap of the SnO₂ shells. Using photocatalytic mineralization of organic dye molecules as model reactions, we show that the interband and plasmonic intraband hot carriers exhibit drastically distinct photocatalytic behaviors in terms of charge transfer pathways, excitation power dependence, and apparent photonic efficiencies. The insights gained from this work form an important knowledge foundation guiding the rational optimization of hot carrier-driven chemical transformations on nanostructured metal-semiconductor hybrid photocatalysts.

Introduction

The idea of exploiting photoexcited charge carriers in semiconductor photocatalysts to trigger interfacial chemical transformations dates back to early 1970s when Fujishima and Honda discovered the electrochemical photolysis of water on ultraviolet (UV)-illuminated TiO₂ electrodes.¹ The charge carriers generated upon excitonic excitations of nanostructured semiconductors have been harnessed to drive a diverse set of important photocatalytic reactions, enabling judicious utilization of the solar energy for clean fuel production, environmental remediation, and biomedical applications.²⁻⁶ Success in optimizing semiconductor-based photocatalysis essentially relies on our capabilities to suppress the recombination of photoexcited charge carriers and to fine-tune the light-absorbing behaviors of the photocatalysts spanning the entire solar spectrum. Although photochemically stable oxide semiconductors with wide band gaps above ~ 3.0 eV,²⁻¹¹ such as TiO₂ and SnO₂, constitute the most extensively used photocatalysts so far, they only absorb the UV light that accounts for less than 5 % of all incident solar radiation. To extend the spectral range of light absorption into the visible (42-43 % of solar radiation) and infrared (52-55 % of solar radiation), wide-band-gap semiconductors have been either chemically doped⁸⁻¹³ to fine-engineer their electronic band structures and surface trap

states or coupled with visible- and infrared-absorbing photosensitizers, most commonly dye molecules and quantum dots,^{10, 13-16} to optimize the light-harvesting and charge separation processes. Here we explore alternative pathways of creating energetic charge carriers under excitations by photons with energies far below the semiconductor band gaps using colloidal Au@SnO₂ core-shell nanoparticles (CSNPs) as an optically tunable metal-semiconductor hybrid photocatalyst. Instead of directly exciting the excitons in the SnO₂ shells by the UV light, we optically excite the plasmonic electron oscillations and the d→sp interband transitions of the Au cores in the visible and near-infrared to create energetic charge carriers exploitable for photocatalytic mineralization of organic dye molecules in aqueous solutions.

Metal-semiconductor hybrid heteronanostructures with deliberately designed architectures have emerged as particularly promising candidate materials for fine-optimizing photocatalysis.¹⁷⁻²⁵ Optical excitation of free electron oscillations in metallic nanoparticles, also known as plasmon resonances, produces nonthermal distribution of hot electrons that can be injected into unoccupied orbitals of the molecules adsorbed on the nanoparticle surfaces to induce a series of unconventional molecular transformations.²⁶⁻³² The plasmonic hot carriers in metals are fundamentally distinct from the excitons in semiconductors in terms of excited-state lifetimes, decay pathways, energy landscapes, and transfer dynamics,^{21, 28, 31} representing a paradigm-shift in charge carrier-driven photocatalysis. When a plasmonically excited metal nanoparticle is in contact with a semiconductor, the energetic hot electrons may be either transferred from the metal to the semiconductor before becoming thermalized (the thermal

^a Department of Chemistry and Biochemistry, University of South Carolina, Columbia, South Carolina 29208, United States. Email: wang344@mailbox.sc.edu

^b School of Chemistry and Chemical Engineering, Jiangsu University, Zhenjiang, Jiangsu 212013, China. Email: xfu@ujs.edu.cn

†Electronic Supplementary Information (ESI) available.
See DOI: 10.1039/x0xx00000x

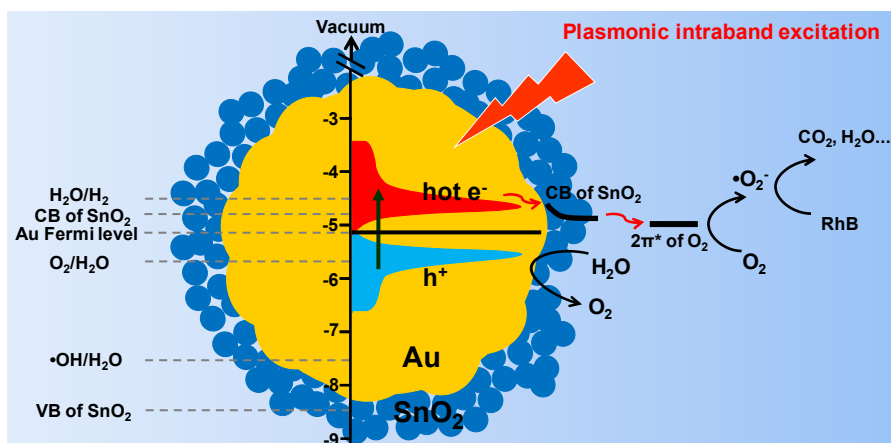


Figure 1. Schematic illustration of the hot electron-driven photocatalytic mineralization of RhB on Au@SnO₂ CSNPs upon plasmonic intraband excitations. The band positions of CB and VB of SnO₂, the Fermi level of Au, and the standard potentials of several redox couples are shown using an energy scale of electron volts (eV) and the vacuum level as the reference.

carrier relaxation occurs on a timescale ranging from 100 fs to 1 ps)^{22, 23, 31, 33, 34} or directly excited in the conduction band (CB) of the semiconductor,³⁵ enabling effective spatial charge separation across the metal-semiconductor heterojunctions. Although the plasmonic hot electrons are short-lived with intrinsic lifetimes in the range of 1-100 fs,^{28, 31} they may become significantly longer-lived when transferred from metals to semiconductors, as demonstrated on Au/TiO₂ heteronanostructures.²² The plasmon-mediated photocatalysis on metal-semiconductor hybrid heteronanostructures, however, should not always be interpreted solely in the context of plasmonic hot carriers. When the plasmon resonances spectrally overlap with the interband absorption of the semiconductors, the metallic nanoparticles may also serve as plasmonic antennas that enhance the photo-generation of charge carriers in nearby semiconductors through either a radiative pathway boosted by the enhancement of local electromagnetic field (LEMF)³⁶⁻³⁸ or a nonradiative pathway involving plasmon-induced resonance energy transfer (PIRET).^{19, 39} Therefore, the photocatalytic behaviors of metal-semiconductor heteronanostructures may be dictated by plasmon resonances through multiple mechanistically distinct pathways, depending on the architectural arrangement of the metal and semiconductor domains, the spectral overlap between the plasmon resonances and the interband absorption of the semiconductor, the alignment of the semiconductor bands with respect to the metal Fermi level, and the energy of the excitation photons.

Au@SnO₂ CSNPs exhibit a unique set of optical characteristics, rendering them an ideal materials system for systematic investigations of the hot carrier-driven, multimodal photocatalysis on metal-semiconductor heteronanostructures. First, the Au cores serve as plasmonic photosensitizers with light absorption properties fine-tunable over a broad spectral range well-below the SnO₂ band gap (3.6-3.8 eV).⁴⁰ Second, the energetically favorable alignment of the CB of SnO₂ with respect to the Fermi level of Au enables efficient transfer of the plasmonic hot electrons to the CB of SnO₂, effectively separating the hot electrons from the holes across the

Au/SnO₂ interfaces and making the excited states longer-lived. Third, the negligible spectral overlap between the plasmon resonances and the interband absorption of SnO₂ enables us to study the plasmonic hot carrier-driven photocatalysis without complication by the radiative LEMF and the nonradiative PIRET effects. Fourth, the intrinsic d→sp interband transitions of Au occur in an intermediate spectral region with energies above the plasmon resonances but below the band gap of SnO₂. It has been demonstrated that the hot carriers derived from the interband transitions of Au nanoparticles can also be harnessed to drive photocatalytic reactions,⁴¹⁻⁴⁵ providing an alternative pathway for photocatalysis distinct from those mediated by semiconductor excitons and plasmonic hot electrons. Use of Au@SnO₂ CSNPs as the photocatalysts allows us to systematically compare the photocatalytic behaviors of the hot carriers derived from the d→sp interband transitions vs. the intraband plasmonic excitations.

Results and discussion

Figure 1 schematically illustrates the plasmonic hot carrier generation, separation, and transfer processes involved in the photocatalytic mineralization of rhodamine B (RhB) on Au@SnO₂ CSNPs under aerobic reaction conditions. Photoexcitation of the plasmon resonance generates a nonthermal distribution of hot electrons above the Fermi level of Au, while leaving holes below the Fermi level. Because the lower edge of SnO₂ CB (-4.8 eV vs. vacuum) lies only about 0.3 eV above the Fermi level of Au (-5.1 eV vs. vacuum),⁴⁶ the injection of hot electrons into the CB of SnO₂ is energetically favorable. The molecular O₂ adsorbed on SnO₂ surfaces is highly electrophilic⁴⁷ and can readily accept the electrons in the CB of SnO₂ into its antibonding π* orbitals to form •O₂⁻ radicals,⁴⁸ a reactive oxygen species (ROS) capable of oxidizing aromatic organic compounds into fully mineralized small molecules, such as CO₂ and H₂O.⁶ It has been well-documented in the literature that the •O₂⁻ radicals may further evolve into other ROS, such as •OH and •OOH, which are also involved in the photocatalytic mineralization of organic compounds.⁶

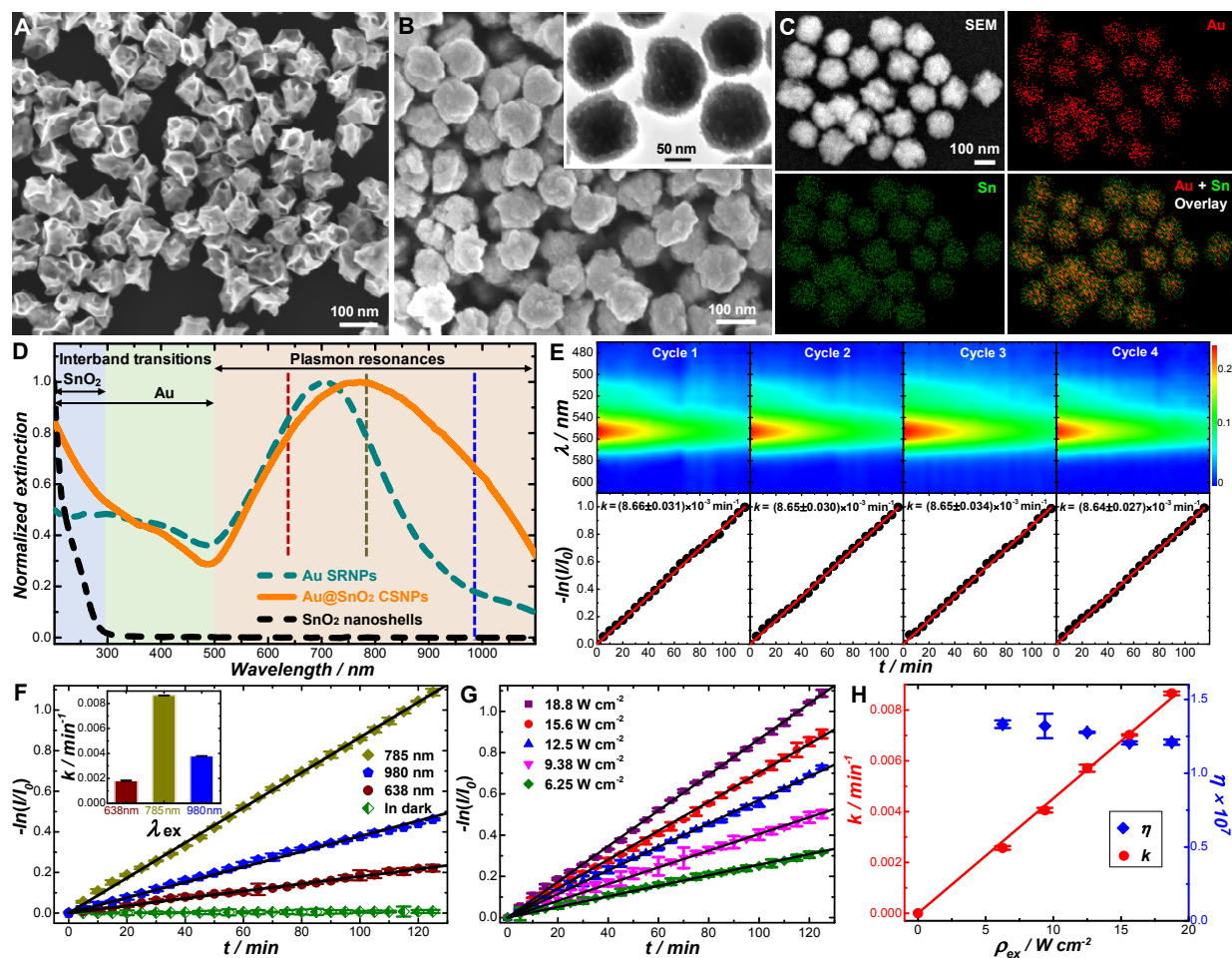


Figure 2. (A) SEM image of Au SRNPs with an average diameter of ~ 96 nm. (B) SEM and (inset) TEM images of Au@SnO₂ CSNPs with an average core size of ~ 96 nm and shell thickness of ~ 17 nm. (C) SEM image and EDS elemental maps of Au and Sn of Au@SnO₂ CSNPs. (D) Optical extinction spectra of colloidal Au SRNPs, Au@SnO₂ CSNPs, and polycrystalline SnO₂ nanoshells. The spectral regions for the intraband plasmon resonances of Au, the d \rightarrow sp interband transitions of Au, and VB \rightarrow CB interband transitions of SnO₂ are shaded in light orange, green, and blue, respectively. The vertical dash lines indicate the wavelengths (638, 785, and 980 nm) of the excitation lasers used for photocatalytic reactions. (E) Kinetics of photocatalytic mineralization of RhB on Au@SnO₂ CSNPs ($\lambda_{\text{ex}} = 785$ nm; $\rho_{\text{ex}} = 18.8$ W cm⁻²) in O₂-saturated aqueous solutions over 4 cycles of reactions. The upper panels showed the temporal evolution of absorption spectra and the lower panels showed the temporal evolution of $-\ln(I/I_0)$. (F) Temporal evolution of $-\ln(I/I_0)$ during the photocatalytic mineralization of RhB on Au@SnO₂ CSNPs in O₂-saturated solutions at λ_{ex} of 633, 785, and 980 nm with ρ_{ex} of 18.8 W cm⁻². The inset panel showed the values of k obtained from least squares curve fitting for different λ_{ex} . (G) Temporal evolution of $-\ln(I/I_0)$ at λ_{ex} of 785 nm with varying ρ_{ex} . (H) ρ_{ex} -dependence of k and η . The error bars in panels F, G, and H represented the standard deviations obtained from 3 experimental runs under each condition.

We synthesized Au@SnO₂ CSNPs by growing polycrystalline SnO₂ nanoshells on Au surface-roughened nanoparticles (SRNPs) through seed-mediated hydrolysis of Na₂SnO₃.⁴⁹⁻⁵¹ While conventional spherical or quasi-spherical Au nanoparticles exhibit rather limited plasmonic tunability and weak local-field enhancements, introduction of nanoscale surface roughness to Au nanoparticles remarkably enhances the plasmonic tunability over a broad spectral range and drastically amplifies the LEMF on particle surfaces.^{52, 53} We synthesized Au SRNPs using a kinetically controlled, seed-mediated growth method.^{52, 53} Figure 2A shows a

representative scanning electron microscopy (SEM) image of Au SRNPs with an average diameter of ~ 96 nm. The particle surfaces are rich of sharply curved sites, which serve as the near-field “hot-spots” not only exploitable for plasmon-enhanced spectroscopy⁵² but also beneficial to the surface accumulation of plasmonic hot electrons. Coating of each Au SRNP with a polycrystalline SnO₂ shell upon hydrolysis of Na₂SnO₃ was clearly manifested by significant increase of particle size and modification of the surface morphology (Figure 2B). Transmission electron microscopy (TEM) revealed that each Au@SnO₂ CSNP exhibited a well-defined core-shell

heterostructure (inset of Figure 2B). The characteristic energy-dispersive spectroscopy (EDS) signals of the Au, Sn, and O elements in the nanoparticle samples were all clearly identified and spectroscopically well-resolved (Figure S1 in ESI), allowing us to quantify the Au/Sn stoichiometric ratios and further confirm the Au-core and SnO₂-shell structure through EDS-elemental mapping (Figure 2C). High-resolution TEM (HRTEM) showed that the SnO₂ nanoshells were polycrystalline in nature, displaying a nanoporous network consisting of interconnected primary SnO₂ nanocrystals, each of which was 4–6 nm in size (Figure S2 in ESI). The Au cores could be completely etched while keeping the SnO₂ shells structurally intact by exposing the Au@SnO₂ CSNPs to KI/I₂ (Figure S3 in ESI), a chemical etchant that selectively dissolves Au,⁵⁴ indicating that the surfaces of the Au cores were accessible by small molecules due to the nanoporous nature of the SnO₂ shells. Powder X-ray diffraction (PXRD) results confirmed that the as-synthesized Au@SnO₂ CSNPs were composed of two distinct crystalline components, tetragonal SnO₂ and face-centered cubic Au (Figure S4 in ESI). The small crystalline sizes of SnO₂ caused significant broadening of the SnO₂ diffraction peaks. The average size of the primary SnO₂ nanocrystals was estimated to be 4.5 nm using the Scherrer equation,⁵⁵ in agreement with the HRTEM observations.

We used optical extinction spectroscopy to characterize the optical properties of the Au SRNPs, Au@SnO₂ CSNPs, and polycrystalline SnO₂ nanoshells (Figure 2D). When colloidal Au SRNPs (average diameter of 96 nm) were dispersed in water, their extinction spectral features were dominated by a broad peak centered at ~707 nm, which was assigned to the characteristic dipolar plasmon resonance.⁵² The plasmon peak significantly red-shifted to ~772 nm and became further broadened after coating the Au SRNPs with nominally ~17 nm thick SnO₂ shells because the refractive index of SnO₂ (1.77) was higher than that of water (1.33).⁴⁹ Meanwhile, colloidal Au@SnO₂ CSNPs strongly absorbed the UV light at wavelengths shorter than ~320 nm due to the VB→CB interband transitions of SnO₂. The optical excitation of d→sp interband transitions of Au occurred at energies higher than ~2.3 eV,⁵⁶ giving rise to a spectral feature in the visible at wavelengths below ~530 nm. SnO₂ nanoshells without the Au cores appeared optically transparent throughout the visible and near-infrared regions. According to the UV-Visible diffuse reflectance spectrum, the band gap of the polycrystalline SnO₂ nanoshells was determined to be ~3.7 eV (Figure S5 in ESI), which was in agreement with the band gap values of bulk SnO₂ reported in the literature.^{46, 57} Because the sizes of the primary SnO₂ nanocrystals were larger than the exciton Bohr radius of SnO₂ (2.7 nm),⁵⁷ we did not observe the widening of the SnO₂ band gap due to quantum confinement effects.

We excited the plasmonic electron oscillations in colloidal Au@SnO₂ CSNPs using a continuous-wave diode laser with an emission wavelength at 785 nm (photon energy: 1.6 eV) to drive the photocatalytic mineralization of RhB in O₂-saturated aqueous solutions (see experimental details in ESI). To avoid the photothermal effects caused by laser illumination, the temperature of the bulk solution was maintained at 25 ± 0.2 °C using a water bath with circulating water. We monitored the reaction kinetics using UV-visible absorption spectroscopy by tracking the temporal intensity evolution of the characteristic absorption peak of RhB

centered at 553 nm (Figure 2E). Under 785 nm excitations, the decay of plasmonic electron oscillations resulted in energetic hot electrons distributed up to 1.6 eV above the Fermi level of Au. A significant population of the hot electrons had sufficient energy to overcome the Schottky barrier across the Au-SnO₂ interfaces to get injected into the CB of SnO₂, followed by transfer into the π* orbital of the molecular O₂ adsorbed on SnO₂ surfaces to form ·O₂⁻. A potentially more efficient charge separation pathway involves the direct excitation of hot electrons in the CB of SnO₂ shell, leaving the holes in the Au core. However, whether such direct excitation occurs on the Au@SnO₂ CSNPs upon plasmonic excitations still remains an open question. The SnO₂ shells and the surface-adsorbed O₂ served as the electron relays to mediate the photocatalytic reactions. Au@SnO₂ CSNPs showed no photocatalytic activity under anaerobic conditions when the reaction solution was continuously purged with N₂ (Figure S6 in ESI). Au SRNPs without the SnO₂ shells appeared inactive toward the aerobic photocatalytic RhB mineralization, primarily due to limited life-time of the hot electrons generated in Au and the energetically unfavorable adsorption of O₂ on Au surfaces.⁵⁸ The SnO₂ shells without the Au cores were also photocatalytically inactive at 785 nm excitation, strongly indicating that the aerobic mineralization of RhB was indeed driven by photoexcited plasmonic hot electrons.

Although the photocatalytic mineralization of RhB is a mechanistically complex multistep process,⁶ the decolorization of RhB was observed to follow a simple first-order rate law (Figure 2E), strongly suggesting that the rate-limiting step was most likely the oxidation of RhB by ·O₂⁻ radicals rather than the interfacial transfers of hot electrons. Assuming the decolorization of RhB as the initial elementary step during ·O₂⁻-driven mineralization of RhB, the rate law can be described using the following equation:

$$-\frac{d[\text{RhB}]}{dt} = k' [\text{RhB}][\cdot\text{O}_2^-] \quad (1),$$

where k' is the second-order rate constant. Under our experimental conditions, we continuously purged the reaction solutions with O₂ to ensure that the solutions were saturated with dissolved O₂. The overall reaction rate was essentially modulated by ·O₂⁻ at its steady state concentration, which was related to both the excitation power and the concentration of dissolved O₂. Therefore, the reaction kinetics at a specific excitation power could be further simplified as a pseudo-first-order rate law described by the following equation:

$$-\ln \frac{[\text{RhB}]}{[\text{RhB}]_0} = -\ln \frac{I}{I_0} = k \times t \quad (2),$$

where I_0 is the intensity of the absorption peak at 553 nm before the reactions, and I is the peak intensity evolving over time, which is proportional to RhB concentration according to the Beer-Lambert Law. The apparent first-order rate constant, k , which corresponded to the slopes of the $-\ln(I/I_0)$ vs. t plots, could be obtained by least squares curve fitting (Figure 2E). The Au@SnO₂ CSNPs exhibited long-term structural stability without any observable photocorrosion during the photocatalytic reactions (Figure S7 in ESI) and could be recycled multiple times with negligible deterioration in activity (Figure 2E). While the hot electron-driven ·O₂⁻ generation occurred on the SnO₂ surfaces, the plasmonic hole-driven reactions occurred probably on the surfaces of the Au cores, resulting in the

O₂ evolution from water as illustrated in Figure 1. Neither the injection of plasmonic holes into the valence band (VB) of SnO₂ nor the hole-driven formation of ·OH radicals was likely to happen because of insufficient energies of the plasmonic holes.

To further verify that the photocatalytic reactions were indeed driven by plasmonic hot electrons, we systematically compared the reaction kinetics at various excitation wavelengths, λ_{ex} and excitation power densities, ρ_{ex} . In Figure 2F, we compared the rate constants, k , excited by three different lasers at λ_{ex} of 638, 785, and 980 nm, respectively, with the same ρ_{ex} of 18.8 W cm⁻². The photocatalytic reactions followed pseudo-first-order kinetics at all three λ_{ex} , whereas almost no reaction occurred in the dark over extended time periods up to a few days. Maximal reaction rates were achieved when the excitation laser was on resonance with the plasmonic electron oscillations. As the excitation laser was detuned to be off-resonance with the plasmons, k significantly decreased. Figure 2G shows the excitation power dependence of k at λ_{ex} of 785 nm. Although k increased with ρ_{ex} , the reactions always obeyed the pseudo-first-order rate law, suggesting that variation of ρ_{ex} did not change the reaction mechanisms. k increased linearly with ρ_{ex} when ρ_{ex} was varied in the range from 0 to 18.8 W cm⁻² (Figure 2H), indicating that the reactions were driven by photoexcited charge carriers with negligible complication caused by plasmonic photothermal effects under the current experimental conditions.^{26, 28, 29} We further calculated the apparent photonic efficiency, η , of the hot carrier-driven photocatalytic reactions, which was defined

as the ratio between the number of RhB molecules degraded and the number of photons incident on the samples during 1-hour reaction time (see details in ESI). As shown in Figure 2H, η was independent of ρ_{ex} in this power range, exhibiting values on the order of 10⁻⁷. The quantum efficiency, which refers to the ratio between the number of hot electrons harnessed for the reactions and the number of photons absorbed by the photocatalysts, was estimated to be one to two orders of magnitude higher than η for several reasons. First, at λ_{ex} of 785 nm, only ~30 % of the incident photons were absorbed or scattered by the colloidal photocatalysts in the light illumination path under our experimental conditions. Second, because of relatively large particle sizes, a significant portion of the incident photons were scattered rather than being absorbed by the Au@SnO₂ CSNPs. The size-dependent light absorption and scattering properties of Au SRNPs were experimentally studied in great detail and further corroborated by finite difference time domain (FDTD) calculations in a paper we previously published.⁵² Third, we assumed that one hot electron was utilized to induce the decolorization of one RhB molecule when calculating η . This assumption led to significant underestimate of the quantum efficiency because multiple copies of hot electron-induced ROS were needed to degrade one RhB molecule into fully mineralized products.⁶

The plasmon resonance wavelengths of Au@SnO₂ CSNPs could be fine-tuned across the visible and near-infrared with respect to the wavelengths of the excitation lasers by simply varying the sizes

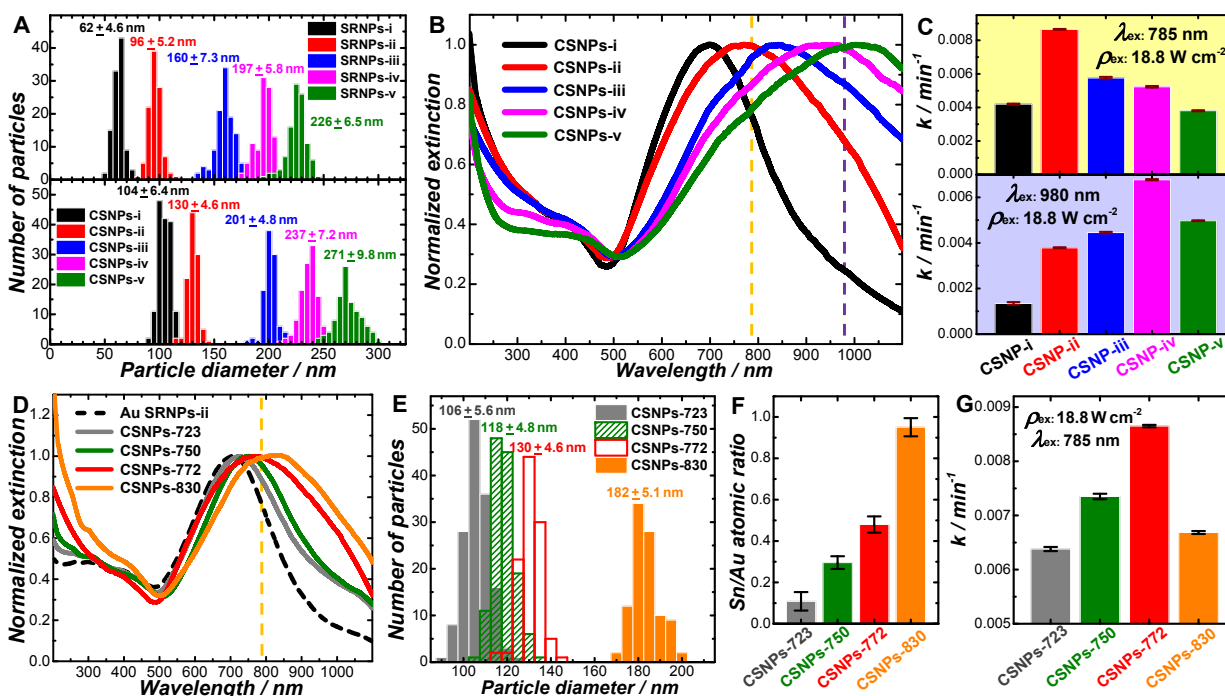


Figure 3. (A) Size distributions of various (upper panel) Au SRNPs and (lower panel) Au@SnO₂ CSNPs. (B) Extinction spectra of Au@SnO₂ CSNPs of various sizes. (C) k of the photo-reactions catalyzed by various Au@SnO₂ CSNP samples in O₂-saturated solutions under the excitations by 785 nm (upper panel) and 980 nm (lower panel) lasers with ρ_{ex} of 18.8 W cm⁻². (D) Extinction spectra of colloidal Au SRNPs-ii and various Au@SnO₂ CSNP samples synthesized using Au SRNPs-ii as the cores. The Au@SnO₂ CSNP samples were denoted as CSNPs-723, CSNPs-750, CSNPs-772, and CSNPs-830, respectively, according to their plasmon resonance peak positions in the extinction spectra. (E) Size distributions and (F) Sn/Au atomic ratios (quantified by EDS) of CSNPs-723, CSNPs-750, CSNPs-772, and CSNPs-830. (G) k of the photo-reactions catalyzed by various Au@SnO₂ CSNPs in O₂-saturated solutions ($\lambda_{\text{ex}} = 785$ nm; $\rho_{\text{ex}} = 18.8$ W cm⁻²).

of the Au cores. We synthesized Au SRNPs with five different average diameters, which were labeled as Au SRNPs-i, SRNPs-ii, SRNPs-iii, SRNPs-iv, and SRNPs-v, respectively, in the order of increasing particle sizes (Figure S8A-S8E in ESI). Both the roughened surface morphology and the feature sizes of the surface textures remained essentially unchanged as the overall particle sizes varied. The plasmon resonance peaks of Au SRNPs progressively red-shifted and became increasingly broadened as the particle size increased (Figure S8F in ESI). We then grew polycrystalline SnO₂ shells on the Au SRNPs to synthesize Au@SnO₂ CSNPs with various average core sizes but similar average shell thicknesses in the range of ~17-22 nm, which were labeled as CSNPs-i, CSNPs-ii, CSNPs-iii, CSNPs-iv, and CSNPs-v, respectively, in the order of increasing core sizes (Figure S9 in ESI). The size distributions of various Au SRNP and Au@SnO₂ CSNP samples were shown in Figure 3A. We consistently observed spectral red-shifts of the plasmon resonance peaks after coating the Au SRNPs with SnO₂ shells (Figure 3B). We observed a general trend at λ_{ex} of both 785 and 980 nm that on-resonance excitations gave rise to highest reaction rates, while the reactions became progressively slower as the plasmon resonances were gradually detuned to be off-resonance with the excitation laser (Figure 3C and Figure S10 in ESI).

An alternative way to tune the plasmon resonances of Au@SnO₂ CSNPs was to vary the thickness of the SnO₂ shells without changing the size of the Au cores. Using Au SRNPs-ii as the cores, we synthesized four Au@SnO₂ CSNP samples with various shell thicknesses (Figure S11 in ESI), which were labeled as CSNPs-723, CSNPs-750, CSNPs-772, and CSNPs-830, respectively, according to the wavelengths of their plasmon resonance peaks. As the shell thickness increased, the plasmon resonances of the Au@SnO₂ CSNPs progressively shifted to longer wavelengths (Figure 3D). The size distributions and the Sn/Au atomic ratios (quantified by EDS) of the Au@SnO₂ CSNPs were shown in Figure 3E and 3F, respectively. Among the four Au@SnO₂ CSNP samples we investigated, CSNPs-772 exhibited the highest photocatalytic activity (Figure 3G and Figure S12 in ESI) primarily due to the closest energy match between the plasmon resonance and the 785 nm excitation laser, further verifying that the photocatalytic behaviors of Au@SnO₂

CSNPs under visible and near-infrared excitations in aerobic environment were essentially dictated by plasmonic hot electrons.

The plasmonic behaviors of an ideal metal can be fully described in the context of the Drude model, which only considers the contribution of free electrons to the dielectric functions of the metal. However, the band structures of a real metal are typically more complex than the free electron model because the contribution of interband transitions should also be taken into considerations.^{41, 56, 59} For metallic Au, the sp-band, which expands across the Fermi level, resembles the dispersion of free electrons. Therefore, the plasmonic excitations essentially refer to the intraband electronic transitions within the sp-band, whereas the electrons in the filled d-band are excited to the empty states in the sp-band upon excitations of interband transitions.⁵⁶ In contrast to conventional spherical Au nanoparticles whose intraband plasmon resonances significantly overlap with the d→sp interband transitions, Au@SnO₂ CSNPs exhibited tunable plasmon resonances in the visible and near-infrared at energies far below the energy threshold for the interband excitation of Au (~ 2.3 eV). Here we selectively excited the d→sp interband transitions of Au at 445 nm (2.8 eV) on the higher-energy side of the plasmon resonances but below the band gap of SnO₂. As illustrated in Figure 4, the energy distribution profiles of the interband hot carriers are distinct from those of the plasmonic hot carriers. Optical excitation of the d→sp interband transitions creates energetic hot holes in the d-band, about 2.3 eV below the Fermi level of Au, while the photoexcited electrons are distributed near the Fermi level and are thus typically not as energetic as the holes. The interband hot holes can oxidize water on Au core surfaces to form ·OH radicals, which also serve as a ROS that induces the mineralization of RhB. At λ_{ex} of 445 nm, the energy of the excitation photons exceeds the energy threshold for interband transitions by ~ 0.5 eV, creating photoexcited electrons in the sp-band distributed up to ~ 0.5 eV above the Fermi level. Therefore, some interband hot electrons can be injected into the CB of SnO₂ and further transferred into the π^* orbitals of the molecular O₂ adsorbed on SnO₂ surfaces to form ·O₂⁻ radicals. Optical excitation of the d→sp interband transitions of the Au cores in the Au@SnO₂ CSNPs allows us to utilize both the hot holes and

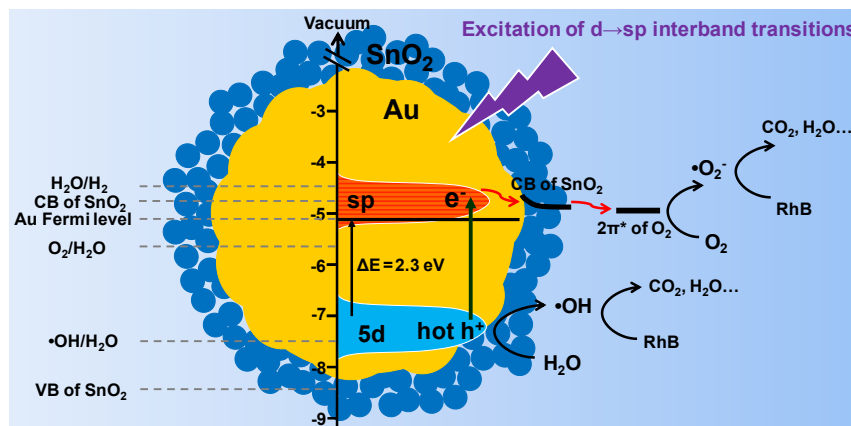


Figure 4. Schematic illustration of the hot hole- and electron-driven photocatalytic mineralization of RhB on Au@SnO₂ CSNPs upon excitations of the d→sp interband transitions in Au. The band positions of CB and VB of SnO₂, the Fermi level of Au, and the standard potentials of several redox couples are shown using an energy scale of eV and the vacuum level as the reference.

electrons to drive the photocatalytic mineralization of RhB under aerobic reaction conditions, whereas upon intraband plasmonic excitations, only the hot electrons can be harnessed for photocatalysis.

We further studied the power-dependence of the interband hot carrier-driven RhB mineralization under aerobic conditions at λ_{ex} of 445 nm using Au@SnO₂ CSNPs-ii (Au diameter of ~ 96 nm and shell thickness of ~ 17 nm) as the photocatalysts. Polycrystalline SnO₂ nanoshells were observed to be photocatalytically inactive at λ_{ex} of 445 nm (Figure S13 in ESI) because the excitation energy was insufficient for the excitonic excitations of SnO₂. The interband hot carrier-driven reactions followed pseudo-first-order kinetics (Figure 5A), analogous to the reactions driven by plasmonic hot electrons. However, k of the interband hot carrier-driven reactions exhibited a power dependence strikingly distinct from the linear power dependence observed on the plasmon-driven reactions. As shown in Figure 5B, k increased linearly with the excitation power at ρ_{ex} below ~ 2 W cm⁻². As ρ_{ex} further increased, significant deviation from linear power dependence was observed and k asymptotically approached a plateau at ρ_{ex} above ~ 6 W cm⁻². In the weak excitation ($\rho_{\text{ex}} < 2$ W cm⁻²) regime where the linear power dependence still held, η was independent of ρ_{ex} . The values of η were on the order of 10^{-6} at low ρ_{ex} , about one order of magnitude higher than those of the plasmonic hot electron-driven reactions. However, η significantly dropped as ρ_{ex} further increased, decreasing by more than 10 times when reaching a sufficiently high ρ_{ex} regime. The thermalization or recombination of the hot carriers,

whose rates had a second-order dependence on light intensity, became faster as ρ_{ex} increased, resulting in decreased hot carrier transfer efficiency and thus lower η . Our results strongly indicate that direct excitation of d \rightarrow sp interband transitions provides a more efficient pathway of absorbing light and thus producing hot carriers than the intraband plasmonic excitations, even though the interband hot carriers typically have lower kinetic energies than those of plasmonic hot electrons.⁴¹ Previous studies on hot carrier-mediated photo-corrosion of Au nanorods and photocatalytic cyclization of alkynylphenols also suggested that the interband transitions were more efficient in generating hot carriers than the intraband plasmonic excitations,⁴¹ which was echoed by our observations though our system was entirely different in terms of both materials and reactions.

The electron-driven photocatalytic mineralization of RhB required surface adsorbed molecular O₂, and thus could be inhibited by eliminating O₂ in the reaction mixtures. When the solutions were continuously purged with N₂ to create an anaerobic reaction environment, the plasmonic hot electron-driven reaction at λ_{ex} of 785 nm was completely suppressed (Figure 5C and Figure S6 in ESI). At λ_{ex} of 445 nm, the photocatalytic reactions occurred under both aerobic and anaerobic reaction conditions. However, the reaction became significantly slower under the anaerobic conditions because the electron-driven reaction pathway was inhibited due to the absence of O₂ and the mineralization of RhB was driven solely by the interband hot holes (Figure 5C). The hot hole-driven reactions in anaerobic environments also proceeded

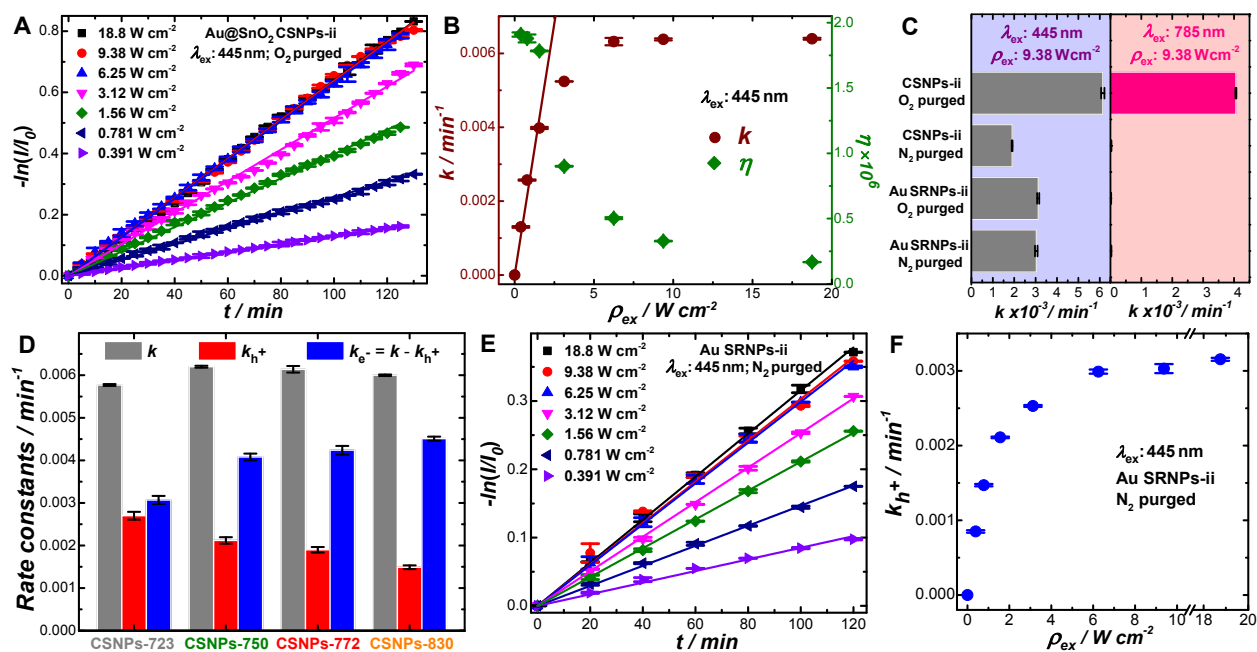


Figure 5. (A) Temporal evolution of $-\ln(I/I_0)$ during the photo-mineralization of RhB catalyzed by Au@SnO₂ CSNPs-ii in O₂-saturated solutions at λ_{ex} of 445 nm with different ρ_{ex} . (B) ρ_{ex} -dependence of k and η at λ_{ex} of 445 nm. (C) k of the photo-reactions catalyzed by the Au@SnO₂ CSNPs-ii and Au SRNPs-ii at λ_{ex} of 445 nm and 785 nm lasers with a ρ_{ex} of 9.38 W cm⁻² in O₂-saturated and deoxygenated (N₂-purged) solutions. (D) Comparison of k , k_{h^+} , and $k_{\text{e}^-} = k - k_{\text{h}^+}$ for the photocatalytic mineralization of RhB ($\lambda_{\text{ex}} = 445$ nm; $\rho_{\text{ex}} = 9.38$ W cm⁻²). (E) Temporal evolution of $-\ln(I/I_0)$ during the photo-mineralization of RhB catalyzed by Au SRNPs-ii in deoxygenated solutions λ_{ex} of 445 nm with different ρ_{ex} . (F) Excitation power dependence of k_{h^+} for the photo-mineralization of RhB catalyzed by Au SRNPs-ii in deoxygenated solutions λ_{ex} of 445 nm.

following a pseudo-first-order rate law (Figure S14 in ESI), which allowed us to obtain the apparent rate constant for the hole-driven reactions, k_h^+ . The apparent rate constant for the reactions driven by the interband electrons, k_e^- , was calculated by subtracting k_h^+ from k , the rate constants of the overall reactions driven by both electrons and holes in O₂-saturated solutions at λ_{ex} of 445 nm. In Figure 5D, we compared the k , k_h^+ , and k_e^- for the photocatalytic mineralization of RhB ($\lambda_{\text{ex}} = 445$ nm; $\rho_{\text{ex}} = 9.38$ W cm⁻²) on Au@SnO₂ CSNPs with the same core sizes but different shell thicknesses. Although the plasmon resonances progressively red-shifted as the shell thickness increased (Figure 3D), the values of k appeared similar among various Au@SnO₂ CSNP samples, indicating that these reactions were indeed driven by the interband hot carriers, independent of the plasmon resonances. Interestingly, k_h^+ decreased as the shell thickness increased because thicker SnO₂ shells hindered the diffusion of H₂O molecules to the surfaces of the Au cores, where the hot hole-driven generation of ·OH occurred. On the other hand, k_e^- increased with the shell thickness because thicker nanoporous shells provided larger surface areas available for O₂ adsorption. The Au@SnO₂ CSNPs exhibited excellent photocatalytic durability under interband excitations at 455 nm in both aerobic and anaerobic environments, and could be recycled for multiple reaction cycles (Figure S15 in ESI). Because the photogenerated ROS, such as ·O₂⁻ and ·OH, were capable of nonselectively oxidizing a large library of aromatic organic molecules into fully mineralized products, we also successfully harnessed the interband and plasmonic hot carriers created in the Au@SnO₂ CSNPs to efficiently drive the mineralization of several other dye molecules, such as rhodamine 6G (R6G), basic blue 12 (BB12), and methylene blue (MB). The molecular structures of the dye molecules were illustrated in Figure S16 in ESI, and detailed kinetic results of the reactions driven by the plasmonic hot electrons and interband hot carriers were shown in Figures S17 and S18, respectively, in ESI.

While the hot electron-driven formation of ·O₂⁻ was mediated by the SnO₂ shells, the hole-driven generation of ·OH occurred directly on Au surfaces, which was verified by the control experiments using Au SRNPs as the photocatalysts. Although Au SRNPs did not exhibit any observable activity toward RhB mineralization under both aerobic and anaerobic conditions upon plasmonic excitations at λ_{ex} of 785 nm, they became photocatalytically active at λ_{ex} of 445 nm (Figure 5C). Both the aerobic and anaerobic reactions were driven by the interband hot holes and proceeded at similar rates. The reactions at λ_{ex} of 445 nm proceeded even more rapidly on Au SRNPs than on Au@SnO₂ CSNPs in anaerobic environments (Figure 5C), because without the SnO₂ shells, the Au surfaces became directly accessible for hole-driven reactions. Au SRNPs exhibited robust photocatalytic activities at λ_{ex} of 445 nm over multiple reaction cycles (Figure S19 in ESI). While the interband hot holes were exploitable for generation of ·OH, the hot electrons in the sp-band were either used to drive the H₂ evolution reaction or injected into reactive intermediate species generated during mineralization of RhB, possibly phenyl radicals, benzoquinone, and quinhydrone. The hot hole-driven reactions catalyzed by Au SRNPs in anaerobic environments obeyed pseudo-first-order kinetics (Figure 5E). The rate of the interband hot hole-driven reactions reached a plateau at ρ_{ex} above ~6 W cm⁻² (Figure

5F), consistent with the power dependence observed on the aerobic reactions catalyzed by Au@SnO₂ CSNPs at λ_{ex} of 445 nm (Figure 5B).

Conclusions

This work provides important photophysical and photochemical insights into the generation, separation, and transfer of photoexcited hot carriers that underpin the multimodal photocatalytic behaviors of metal-semiconductor hybrid heteronanostructures. Au@SnO₂ CSNPs constitute an intriguing hybrid photocatalytic materials system exhibiting fine-tunable plasmon resonances over a broad spectral range spanning much of the visible and near-infrared, enabling us to judiciously shift the plasmon resonances with respect to the energy thresholds for interband transitions of Au and excitonic excitations of SnO₂. Such unique optical tunability offered by Au@SnO₂ CSNPs enables us to deliberately create energetic hot carriers exploitable for photocatalytic mineralization of organic dye molecules by selectively exciting the d→sp interband transitions and the plasmonic electron oscillations in the Au cores at energies well-below the band gap of the SnO₂ shells. Our results show that the interband and plasmonic intraband hot carriers behave differently in terms of transfer pathways, excitation power dependence, and apparent photonic efficiencies when executing their photocatalytic functions. The knowledge gained from this work provides key design principles for the next-generation metal-semiconductor hybrid photocatalysts that can be used to efficiently harness the solar energy to fine-optimize charge carrier-driven photocatalytic molecular transformations.

Experimental

Nanoparticle Synthesis: Au SRNPs with controlled particle sizes were synthesized through kinetically controlled seed-mediated nanocrystal growth following a previous reported protocol.^{52, 53} Au@SnO₂ CSNPs were synthesized by seed-mediated hydrolysis of Na₂SnO₃^{49, 50} using the Au SRNPs as the seeds. The detailed protocols for the nanoparticle synthesis were presented in the ESI.

Characterizations of Nanoparticles: The structures, compositions, and optical properties of the as-synthesized nanoparticles were characterized using SEM, TEM, EDS, PXRD, optical extinction spectroscopy, and diffuse reflectance spectroscopy (see experimental details in the ESI).

Photocatalytic Mineralization of Organic Dye Molecules: The reaction mixtures for the photocatalytic reactions were prepared by mixing colloidal Au@SnO₂ CSNPs with RhB in aqueous solutions at pH ~7 with a total volume of 5 mL in a cylindrical glass vial (1.5 cm in diameter, 4.5 cm in height). The concentrations of colloidal Au@SnO₂ CSNPs and RhB molecules in the reaction mixtures were ~4.8 × 10¹⁰ particles L⁻¹ and 4.2 μM (2.0 mg L⁻¹), respectively. Prior to laser irradiation, the dispersion was kept in dark with magnetic stir for 2 h to establish an adsorption/desorption equilibrium. To avoid the photothermal effects caused by laser illumination, the temperature of the bulk solution was maintained at 25 ± 0.2 °C using a water bath with circulating water. 4 continuous-wave diode lasers purchased from Lasever Inc. (Ningbo, Zhejiang, China) with

the tunable power output in the range of 0–3.0 W and emission wavelengths at 445 nm (model no. LSR445SD), 638 nm (model no. LSR638CP8), 785 nm (model no. LSR785NL), and 980 nm (model no. LSR980NL) were used as the light sources for excitation. The laser beams were collimated with a 4 mm x 4 mm square cross-section and incident vertically from the top surface into the solution. Oxygen or nitrogen was continuously bubbled through the reaction solution from the bottom at a gas pressure of 200 KPa. To monitor the photocatalytic degradation of RhB, the vial containing the reactants and photocatalysts was taken out from the reaction system at certain time intervals and the RhB molecules remaining in the solution were separated from the photocatalysts through centrifugation. The RhB concentration was quantified by UV-visible absorption spectroscopy using a Beckman coulter Du 640 spectrophotometer according to the absorbance at 553 nm (the characteristic absorption peak of RhB). Once the UV-visible absorption spectroscopic measurements were finished, the photocatalysts and the remaining RB molecules were remixed together and subject to further photocatalytic reactions upon exposure to the laser illumination. For the photocatalytic degradation of R6G, BB12, and MB, the reaction kinetics were monitored based on the temporal evolution of the intensities of the characteristic absorption peaks at 530 nm, 635 nm, and 668 nm, respectively. For photocatalytic durability tests, the photocatalysts were recycled through centrifugation after the photo-reactions proceeded for 2 h and then redispersed in 5 mL of RhB dye (2.0 mg L⁻¹) for the next reaction cycle. In each reaction cycle, the reaction progress was tracked by UV-visible absorption spectroscopic measurements with certain time intervals.

Conflicts of interest

There are no conflicts to declare.

Acknowledgements

This work was funded by the United States National Science Foundation (NSF) through a CAREER Award (DMR-1253231). As a visiting postdoctoral scholar, X.F. was partially supported by the Study-Abroad Funds of Jiangsu University (20162673). G.G.L. was partially supported by a SPARC Graduate Research Grant from the University of South Carolina (USC) Office of the Vice President for Research. E.V. was partially supported by a Graduate Assistance in Areas of National Need (GAANN) Fellowship provided by the United States Department of Education through GAANN Award P200A120075. H.W. acknowledges Jiangsu University for Jinshan Distinguished Professorship (Short-Term Visiting Program). This work made use of the X-ray diffraction facilities at the South Carolina SAXS Collaborative supported by the NSF Major Research Instrumentation program (DMR-1428620) and the electron microscopy facilities at the USC Electron Microscopy Center.

Notes and references

1. A. Fujishima and K. Honda, *Nature*, 1972, 238, 37–38.
2. H. Tong, S. X. Ouyang, Y. P. Bi, N. Umezawa, M. Oshikiri and J. H. Ye, *Adv. Mater.*, 2012, 24, 229–251.
3. F. E. Osterloh, *Chem. Soc. Rev.*, 2013, 42, 2294–2320.
4. X. B. Chen, S. H. Shen, L. J. Guo and S. S. Mao, *Chem. Rev.*, 2010, 110, 6503–6570.
5. S. N. Habisreutinger, L. Schmidt-Mende and J. K. Stolarczyk, *Angew. Chem. Int. Edit.*, 2013, 52, 7372–7408.
6. M. R. Hoffmann, S. T. Martin, W. Choi and D. W. Bahnemann, *Chem. Rev.*, 1995, 95, 69–96.
7. H. J. Zhang, G. H. Chen and D. W. Bahnemann, *J. Mater. Chem.*, 2009, 19, 5089–5121.
8. R. Asahi, T. Morikawa, T. Ohwaki, K. Aoki and Y. Taga, *Science*, 2001, 293, 269–271.
9. S. U. M. Khan, M. Al-Shahry and W. B. Ingler, *Science*, 2002, 297, 2243–2245.
10. R. Marschall, *Adv. Funct. Mater.*, 2014, 24, 2421–2440.
11. X. B. Chen, L. Liu, P. Y. Yu and S. S. Mao, *Science*, 2011, 331, 746–750.
12. Z. G. Zou, J. H. Ye, K. Sayama and H. Arakawa, *Nature*, 2001, 414, 625–627.
13. M. Pelaez, N. T. Nolan, S. C. Pillai, M. K. Seery, P. Falaras, A. G. Kontos, P. S. M. Dunlop, J. W. J. Hamilton, J. A. Byrne, K. O'Shea, M. H. Entezari and D. D. Dionysiou, *Appl. Catal. B- Environ.*, 2012, 125, 331–349.
14. W. J. Youngblood, S. H. A. Lee, K. Maeda and T. E. Mallouk, *Acc. Chem. Res.*, 2009, 42, 1966–1973.
15. J. Hensel, G. M. Wang, Y. Li and J. Z. Zhang, *Nano Lett.*, 2010, 10, 478–483.
16. U. Bach, D. Lupo, P. Comte, J. E. Moser, F. Weissortel, J. Salbeck, H. Spreitzer and M. Gratzel, *Nature*, 1998, 395, 583–585.
17. N. Waiskopf, Y. Ben-Shahar and U. Banin, *Adv. Mater.*, 2018, 30, 1706697.
18. K. F. Wu, H. M. Zhu, Z. Liu, W. Rodriguez-Cordoba and T. Q. Lian, *J. Am. Chem. Soc.*, 2012, 134, 10337–10340.
19. S. K. Cushing, J. T. Li, F. K. Meng, T. R. Senty, S. Suri, M. J. Zhi, M. Li, A. D. Bristow and N. Q. Wu, *J. Am. Chem. Soc.*, 2012, 134, 15033–15041.
20. J. Lee, S. Mubeen, X. L. Ji, G. D. Stucky and M. Moskovits, *Nano Lett.*, 2012, 12, 5014–5019.
21. Y. C. Zhang, S. He, W. X. Guo, Y. Hu, J. W. Huang, J. R. Mulcahy and W. D. Wei, *Chem. Rev.*, 2018, 118, 2927–2954.
22. J. S. DuChene, B. C. Sweeny, A. C. Johnston-Peck, D. Su, E. A. Stach and W. D. Wei, *Angew. Chem. Int. Edit.*, 2014, 53, 7887–7891.
23. H. L. Jia, X. M. Zhu, R. B. Jiang and J. F. Wang, *ACS Appl. Mater. Interfaces*, 2017, 9, 2560–2571.
24. J. H. Yang, Y. Z. Guo, R. B. Jiang, F. Qin, H. Zhang, W. Z. Lu, J. F. Wang and J. C. Yu, *J. Am. Chem. Soc.*, 2018, 140, 8497–8508.
25. L. Ma, S. Liang, X. L. Liu, D. J. Yang, L. Zhou and Q. Q. Wang, *Adv. Funct. Mater.*, 2015, 25, 898–904.
26. P. Christopher, H. L. Xin, A. Marimuthu and S. Linic, *Nat. Mater.*, 2012, 11, 1044–1050.
27. S. Linic, U. Aslam, C. Boerigter and M. Morabito, *Nat. Mater.*, 2015, 14, 567–576.
28. M. J. Kale, T. Avanesian and P. Christopher, *ACS Catal.*, 2014, 4, 116–128.

29. S. Mukherjee, F. Libisch, N. Large, O. Neumann, L. V. Brown, J. Cheng, J. B. Lassiter, E. A. Carter, P. Nordlander and N. J. Halas, *Nano Lett.*, 2013, 13, 240-247.
30. L. A. Zhou, D. F. Swearer, C. Zhang, H. Robotjazi, H. Q. Zhao, L. Henderson, L. L. Dong, P. Christopher, E. A. Carter, P. Nordlander and N. J. Halas, *Science*, 2018, 362, 69-72.
31. M. L. Brongersma, N. J. Halas and P. Nordlander, *Nat. Nanotechnol.*, 2015, 10, 25-34.
32. Y. Kim, J. G. Smith and P. K. Jain, *Nat. Chem.*, 2018, 10, 763-769.
33. S. Linic, P. Christopher and D. B. Ingram, *Nat. Mater.*, 2011, 10, 911-921.
34. M. Kim, M. Lin, J. Son, H. X. Xu and J. M. Nam, *Adv. Opt. Mater.*, 2017, 5, 1700004.
35. K. Wu, J. Chen, J. R. McBride and T. Lian, *Science*, 2015, 349, 632-635.
36. H. A. Atwater and A. Polman, *Nat. Mater.*, 2010, 9, 205-213.
37. S. D. Standridge, G. C. Schatz and J. T. Hupp, *J. Am. Chem. Soc.*, 2009, 131, 8407-8409.
38. Z. W. Liu, W. B. Hou, P. Pavaskar, M. Aykol and S. B. Cronin, *Nano Lett.*, 2011, 11, 1111-1116.
39. J. T. Li, S. K. Cushing, J. Bright, F. K. Meng, T. R. Senty, P. Zheng, A. D. Bristow and N. Q. Wu, *ACS Catal.*, 2013, 3, 47-51.
40. S. Gubbala, V. Chakrapani, V. Kumar and M. K. Sunkara, *Adv. Funct. Mater.*, 2008, 18, 2411-2418.
41. J. Zhao, S. C. Nguyen, R. Ye, B. H. Ye, H. Weller, G. A. Somorjai, A. P. Alivisatos and F. D. Toste, *ACS Cent. Sci.*, 2017, 3, 482-488.
42. S. Roy, S. Roy, A. Rao, G. Devatha and P. P. Pillai, *Chem. Mater.*, 2018, 30, 8415-8419.
43. Y. Kim, D. Dumett Torres and P. K. Jain, *Nano Lett.*, 2016, 16, 3399-3407.
44. S. Yu, A. J. Wilson, J. Heo and P. K. Jain, *Nano Lett.*, 2018, 18, 2189-2194.
45. X. Zhang, X. Li, M. E. Reish, D. Zhang, N. Q. Su, Y. Gutiérrez, F. Moreno, W. Yang, H. O. Everitt and J. Liu, *Nano Lett.*, 2018, 18, 1714-1723.
46. M. Gratzel, *Nature*, 2001, 414, 338-344.
47. M. Batzill and U. Diebold, *Prog. Surf. Sci.*, 2005, 79, 47-154.
48. P. Tiwana, P. Docampo, M. B. Johnston, H. J. Snaith and L. M. Herz, *ACS Nano*, 2011, 5, 5158-5166.
49. G. Oldfield, T. Ung and P. Mulvaney, *Adv. Mater.*, 2000, 12, 1519-1522.
50. S. H. Lee, I. Rusakova, D. M. Hoffman, A. J. Jacobson and T. R. Lee, *ACS Appl. Mater. Interfaces*, 2013, 5, 2479-2484.
51. N. Zhou, L. Polavarapu, Q. Wang and Q. H. Xu, *ACS Appl. Mater. Interfaces*, 2015, 7, 4844-4850.
52. Q. F. Zhang, N. Large, P. Nordlander and H. Wang, *J. Phys. Chem. Lett.*, 2014, 5, 370-374.
53. Q. F. Zhang, D. A. Blom and H. Wang, *Chem. Mater.*, 2014, 26, 5131-5142.
54. E. C. Cho, J. Xie, P. A. Wurm and Y. Xia, *Nano Lett.*, 2009, 9, 1080-1084.
55. F. W. Jones, *Proc. R. Soc. Lond. A-Math. Phys. Sci.*, 1938, 166, 0016-0043.
56. A. O. Govorov, H. Zhang, H. V. Demir and Y. K. Gun'ko, *Nano Today*, 2014, 9, 85-101.
57. E. J. H. Lee, C. Ribeiro, T. R. Giraldo, E. Longo, E. R. Leite and J. A. Varela, *Appl. Phys. Lett.*, 2004, 84, 1745-1747.
58. T. V. W. Janssens, B. S. Clausen, B. Hvolbaek, H. Falsig, C. H. Christensen, T. Bligaard and J. K. Norskov, *Top. Catal.*, 2007, 44, 15-26.
59. R. Sundararaman, P. Narang, A. S. Jermyn, W. A. Goddard and H. A. Atwater, *Nat. Commun.*, 2014, 5, 5788.

Table of contents entry:

Au@SnO₂ core-shell nanoparticles exhibit multimodal photocatalytic behaviors dictated by hot carriers derived from plasmonic intraband and d→sp interband transitions, respectively.

